Spatially Resolved Characterization of Residual Stress Induced by Micro Scale Laser Shock Peening(1501)

Hongqiang Chen, Y. Lawrence Yao, Jeffrey W. Kysar, Department of Mechanical Engineering, Columbia University, New York, NY 10027, U.S.A

ABSTRACT

Single crystal Aluminum of (001) orientation were shock peened using laser beam of 12 micron diameter and observed with X-ray micro-diffraction techniques based on a synchrotron light source. The X-ray micro-diffraction affords micron level resolution as compared with conventional X-ray diffraction which has only mm level resolution. The asymmetric and broadened diffraction profiles registered at each location were analyzed by sub-profiling and explained in terms of the heterogeneous dislocation cell structure. For the first time, the spatial distribution of residual stress induced in micro-scale laser shock peening was experimentally quantified and compared with the simulation result obtained from FEM analysis. Difference in material response and microstructure evolution under shock peening were explained in terms of material property difference in stack fault energy and its relationship with cross slip under plastic deformation.

1. INTRODUCTION

Laser shock peening (LSP) has been studied since 1960s. In particular, LSP can induce compressive residual stresses in the target and improve its fatigue life. The beam spot size used is in the order of millimeters and the compressive stress can typically reach a couple of millimeters into the target material [1]. More recently, laser shock processing of Aluminum and Copper using a micron-sized beam has been experimented and shown to significantly improve fatigue performance of the peened targets [2,3]. It has also been shown through FEM simulation results that the micro-scale laser shock peening (LSP) efficiently induces favorable residual stress distributions in metal targets. Thus, the micro-scale laser shock peening (LSP) is a potential technique that can be used to manipulate the residual stress distributions in metal structures with micron-level spatial resolution and thus improve the reliability performances of micro-devices.

However, it is desirable to directly measure strain/stress distributions of the shocked area with that of simulations. Average strain in the depth direction was measured using Cu (111) and (311) reflections with conventional X-ray diffraction (Cu-K_α X-ray source) for overlapping shock processed bulk copper sample and average residual stress was evaluated [2]. However, the spatial resolution of normal X-ray diffraction is typically larger than 0.5mm, which is too large to measure the residual stress/strain distributions in microscale laser shock peening [3]. Recently, by using synchrotron radiation sources, X-ray microdiffraction measurements based on intensity contrast method [4,5] provide the possibility of measuring the region of stress/strain concentration with micron-level spatial resolution in copper thin-film samples by recording the diffraction intensity contrast of the underlying single crystal silicon substrate [6]. The extremely high brightness X-ray beams from synchrotron radiation sources can achieve short sampling time and are focused to micron spot sizes using X-ray optics. The result provides useful information about the strain field distribution in shock processed copper films, but it is difficult to relate the X-ray diffraction intensity contrast with the stress/strain values quantitatively and it is an indirect measurement since the diffraction signal was taken from the silicon substrate and not from the copper thin film itself.

In this paper, by using the X-ray microdiffraction technology, the spatially resolved X-ray diffraction profiles from laser shock peened bulk single crystal Aluminum was recorded for the first time at the micro scale. The spatial distribution of residual stress induced in micro-scale laser shock peening was quantified using the d-spacing formulation and compared with the simulation result obtained from FEM. Also the microstructure evolution and spatial distribution were studied. Thus, this unique measurement provides the possibility to study the residual stress induced by laser shock peening at the micro scale and gives better understanding of microstructure evolution during the process.

2. MATERIAL SELECTION AND EXPERIMENT CONDITION

FCC metals such as Copper, Nickel and Aluminum are routinely used in micro-devices due to their good mechanical and electrical properties and they are also easier to deform under shock peening compared to *BCC* metals. Although polycrystalline metals are more widely used in practice, single crystal metal is ideal for fundamental study. Well-annealed single crystals of 99.999% pure Aluminum (grown by the seeded Bridgman technique) were used for micro scale laser shock peening here. In order to achieve high diffraction intensity, low order orientations of (001) are

chosen for Al samples (surface normal). The Laue diffraction method was used to determine the crystal orientation and the sample was mounted in a three-circle goniometer and cut to size using a wire EDM. Regular machine polishing was used to remove the heat affected zone (HAZ) of cutting surface and electrolytic polishing was applied for all samples to eliminate the residual stress as the final step.

In order to obtain the deformation symmetry, $[\bar{1}10]$ direction in sample surface was determined by Laue diffraction. Laser shock peening was applied along this direction on sample surface. A frequency tripled Q-switched Nd:YAG laser (wavelength 355nm) in TEM_{00} mode was used, the pulse duration was 50 ns, spacing between consecutive pulses along a shock line was 25μm, and pulse numbers were three on each shocked location at 1KHz pulse repetition rate. Laser beam diameter is 12 microns and laser intensity was about 4GW/cm^2. To apply a coating, a thin layer of high vacuum grease (about 10 microns thick) was spread evenly on the polished sample surface, and the coating material, Aluminum foil of 16 microns thick, which was chosen for its relatively low threshold of vaporization, then tightly pressed onto the grease. The sample was placed in a shallow container filled with distilled water around 3 mm above the sample's top surface. Details of micro-scale LSP setup are referred to [2,3].

3. DEFORMATION MEASUREMENT AND FEM VALIDATION

The typical deformed geometry of the shocked region was observed and measured using AFM as seen in Fig. 1(a). The deformation is uniform along the shocked line, which is indicative of a 2-D deformation, and about ±50 microns in the direction perpendicular to the shocked line. The deformation is due to shock pressure and not due to thermal effects since only the coating is vaporized [2,3]. The process was also modeled and solved via finite element analysis (FEM) and the details of FEM follow Zhang and Yao [2]. A commercial FEM code, ABAQUS, was used for the simulation. The spatial and temporal dependent shock pressure was solved numerically and then used as the loading for the subsequent stress/strain analysis. 3D simulation was carried out assuming finite geometry (500 microns in thickness, 1 mm in width, and 2 mm in length). Pulses at overlapped locations with 25 micron spacing were simulated. Shocks are applied on the top surface along a narrow strip in the width direction for three times which equal to the pulse numbers. The bottom surface is fixed in position, while all the other side surfaces are set traction free.

The deformation in depth direction was shown in Fig. 1(b). As seen, the deformation is similarly uniform along the shocked line, which confirms the 2-D deformation observation above. Fig. 1(c) shows the geometry of the shocked line cross-section measured by AFM and compared with FEM simulation results. The simulated profile generally agreed with the result from AFM except the overall depth is slightly larger in simulation than that from AFM measurement perhaps due to slightly overestimated laser absorption. But the general agreement is indicative of the model's validity and the modeling results will be compared with X-ray diffraction measured residual stress in the subsequent sections.

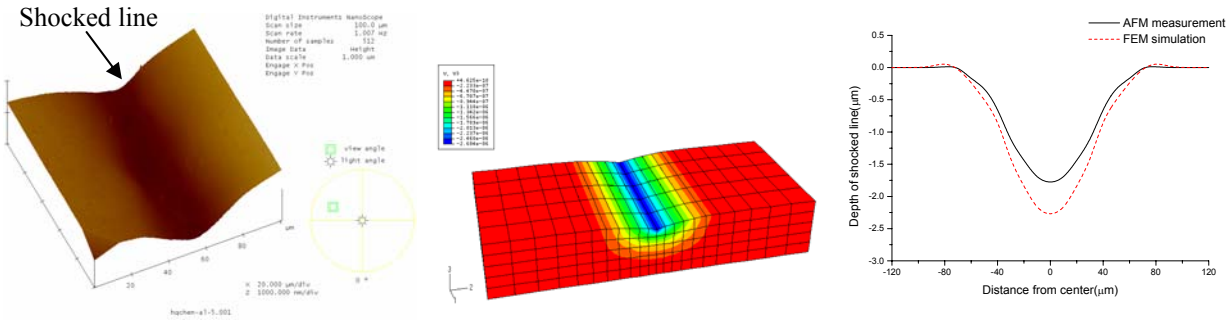

(a) (b) (c)

Figure 1. (a) Measurement of shocked line geometry by AFM(scan area=100×100μm) (b) FEM simulation of depth deformation (in meter) in shock penned sample(500μm×250μm×100μm) (c) Comparison of measured and simulated shocked line profiles for Al sample.

4. SPATIALLY RESOLVED RESIDUAL STRAIN/STRESS MEASUREMENT VIA X-RAY MICRODIFFRACTION

4.1 PRINCIPLES OF X-RAY MICRODIFFRACTION

High brightness X-ray beams are needed for speed and accuracy in X-ray microdiffraction experiments [4,7]. Otherwise, the sampling time need to be extremely long in order to yield meaningful results, and the accuracy can suffer from drifting and noise in such slow and low intensity measurements. For this reason, synchrotron radiation sources are commonly used. The extremely high brightness X-ray beams from synchrotron radiation sources are narrowed down and then focused to micron or submicron spot sizes using X-ray optics such as Fresnel Zone Plates (FZP) or tapered glass capillaries. Focusing lenses for visible light use materials with index of refraction substantially larger than 1. The index of refraction n for most materials at X-ray wavelength is [8]

$$n = 1 - \delta + i\beta \tag{1}$$

where δ is a small number less than 1, which yields the real part of the index of the refraction slightly less than one. Thus, lenses for visible light cannot be used to focus X-rays. Only optics based on diffraction and interference, or on total external reflection can be used for the focusing of X-rays. For X-ray, total reflection occurs when the grazing angle on the surface of an optical medium, such as glass or metal, is less than the critical angle. The reflected X-ray is outside the optical medium. Thus, it is termed total external reflection. The critical angle θ_c for total external reflection is [8]:

$$\theta_c = \sqrt{2\delta} \tag{2}$$

For the lead glass capillary used in this study, the incident bore diameter is about 50μm, the exit bore diameter is about 5μm, and the length is about 8cm. The capillary tube is linear tapered in shape. It is aligned to take in the X-ray beam from the synchrotron beamline, and focuses the beam to a small spot size by total external reflection. At the same time, the gain of the capillary system, defined as the intensity at the exit of the capillary to the intensity at entrance, can be higher than 40 [9]. Both small spot size and increased intensity are desired in X-ray microdiffraction.

4.2 MEASUREMENT SCHEME AND EXPERIMENT SETUP

The extremely high brightness X-ray beams from synchrotron radiation sources (from beamline X20A at National Synchrotron Light Source at Brookhaven National Lab) is first confined into a 0.5×0.5mm beam by slits, then enters a hutch where measurement is taken. The X-ray is concentrated by total reflection as they pass by the tapered glass capillary. The sample is put as near to the capillary as possible to reduce beam radius on target. Beam size was 5 by 7 microns (300 and 30 microns capillary were used in the experiments). The base diffractometer is a commercial Huber two-circle vertical instrument equipped with partial chi (χ) and phi (ϕ) arcs. The samples are mounted on a translation stage with positioning accuracy of ±1μm in the x and y directions in the sample surface. A scintillation X-ray detector is used to monitor the diffraction intensity. A CCD camera is used as monitor to observe the sample surface and help to locate the position of shocked lines on a sample. Data acquisition is controlled by a modified version of the SPEC software package [10]. Monochromatic synchrotron radiation at 8.0 KeV($\lambda = 1.54024\ \mathring{A}$) is used, since it is smaller than the K absorption edge for Al and Cu which are 8.98KeV and 8.3KeV [11] so that the fluorescence radiation would not be excited.

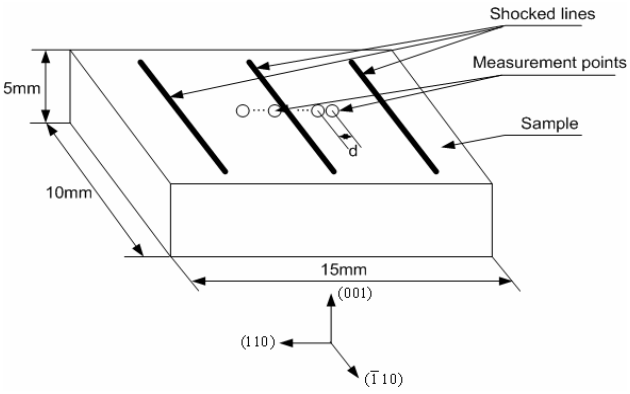

Figure 2. Micro-diffraction measurement arrangement

Multiple measurement points are chosen along a line perpendicular to a shocked line. The spacing between adjacent measurement points starts from 10 μm (when ±100 μm away from the center of the shocked line) and reduces to 5 μm within ±20 μm from the center of the shocked line in order to spatially resolve the residual stress, as shown in Fig. 2. At each position, the corresponding X-ray diffraction profile is recorded and repeated for each shocked line.

For *FCC* metals, the diffraction structure factor for (001) is zero and the reflections are absent [11]. So the (002) and reflections are chosen for measurement. The obtained diffraction profiles will be analyzed and discussed in Section 5. Note these crystallographic

planes are parallel to the shocked surface. Since there are no surface tractions after the shocks are applied, it is expected that the out-of-plane normal stress acting on these planes is zero. The inter-planar distances are then expected to increase slightly to counter the in-plane residual compressive stress. However, the diffraction profiles will be broadened and become asymmetric as a result of the plastic deformation and microstructure change induced by the laser shock peening. It is the broadening and asymmetry will be made use of to estimate the residual stress and this is the essence of the X-ray Scheme 1 and will be fully explained in Sections 5 and 6.

4.3 ASSESSMENT OF MEASUREMENT UNCERTAINTY DUE TO MICRO-BEAM DIVERGENCE

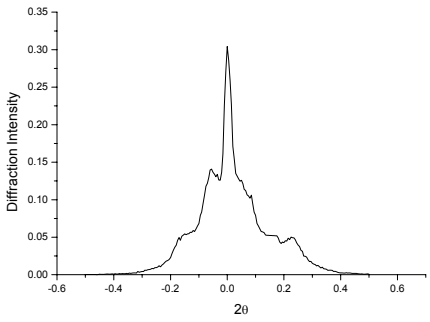

Figure 3. Incident X-ray micro beam profile Full width at half maximum intensity (FWHM)≈0.05°(±0.025°)

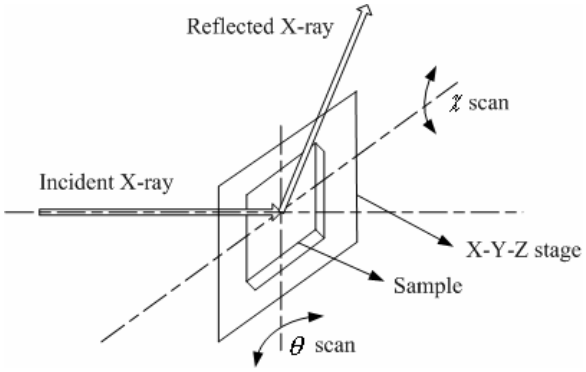

Figure 4. θ and χ scan of sample/stage

The X-ray beam exiting the tapered capillary is divergent and may have non-uniform intensity distribution, whose effect needs to be properly assessed on the measurement accuracy of plastically deformed single crystals in this paper. Fig. 3 shows the X-ray beam profile exiting the tapered capillary used in the experiment which is obtained from a detector scan with very small slit width. As seen, the full width at half maximum intensity (FWHM) is 2γ=0.05°. If such an incident beam fan with total divergence angle equal to 2γ impinges on a perfect single crystal sample surface, only a small central beam portion ($\pm 2\beta$) will make the proper Bragg angle θ for the diffraction, due to the narrow angular bandpass of diffraction [12]. The value of β is typically very small in the order of 10^{-5} degree [11].

In this paper, the single crystal samples underwent plastic deformation which involves small lattice rotations. These rotations differ from location to location depending on the deformation at these locations. As a result, the diffracting lattice plane will not be perfectly parallel to the specimen surface and is tilted off the symmetric Bragg condition by an angle α_i for location *i*, so the central beam vector of incident X-ray is no longer in the Bragg condition and a scan of the diffracted beam will show the peak at $2\theta+\alpha_i$ [12]. As seen from Fig. 4, this error can be eliminated if one scans the diffracted intensity as a function of θ at each measurement location. Assuming that the incident divergent beam shape is a smooth, well-defined function, such as a Gaussian, the mean beam vector will be the most intense ray. Consequently, by rotating the specimen until the maximum intensity is located in the detector, one ensures that the mean beam vector, and not any other, is at the proper angle with respect to the surface.

A similar procedure is followed for setting the proper χ angle at each measurement location, which ensures that the normal vector of the diffracting lattice plane is contained in the same geometrical plane as the incoming and diffracted X-ray beams at each location. Furthermore, for slightly misaligned specimens, rotating in χ can result in compound rotations, where the specimen inclination in the diffractometer plane, θ, can change as well. Thus, the integrated intensity of the relevant reflection in both θ and χ is iteratively optimized during alignment. Once the specimen tilt is properly set, the 2θ value of the peak can be measured by a detector scan in 2θ or by a radial scan where 2θ and θ are stepped at the symmetric 2:1 ratio. The effect of ϕ on measurement accuracy is negligible and is not scanned during the alignment.

5. X-RAY MEASUREMENT RESULT AND PROFILE EVALUATION METHOD

The unsmoothed curves in Fig. 5(a-i) show the diffraction intensity profiles of the (002) Bragg reflection of Al

sample in (001) orientation measured at different locations along a line perpendicular to a shocked line. For example, "-30μm" means this measurement point is at 30μm left of the shocked line center, and "0μm" means at the shocked line center. More points were measured along the line but only nine are presented here to show distinctive changes in profile. The salient features of these line profiles can be summarized as follows:

(a) When the measure point moved across the shock line from left to right (-30μm to +30μm), the line profiles change distinctively from a single symmetric peak to asymmetry with a second peak becoming visible, and finally return to a single symmetric peak.

(b) The vertical line in the profiles represents the theoretical Bragg angle for Al (002) reflection. At ±30μm, the measured profile peak value is almost at the theoretical angle, which in turn represents the shock free regions. When it gets closer to the shocked line center, the peak shifts towards smaller diffraction angles, while a second peak pops up towards larger diffraction angle.

(c) The half-width of the line profiles increases with decreasing distance from the shocked line center. The full width at half maximum (FWHM) of the profile in the center is 3 times greater than the FWHM of the line profile at 30μm away from the center. So the profile is broadened when it gets closer to the shocked region.

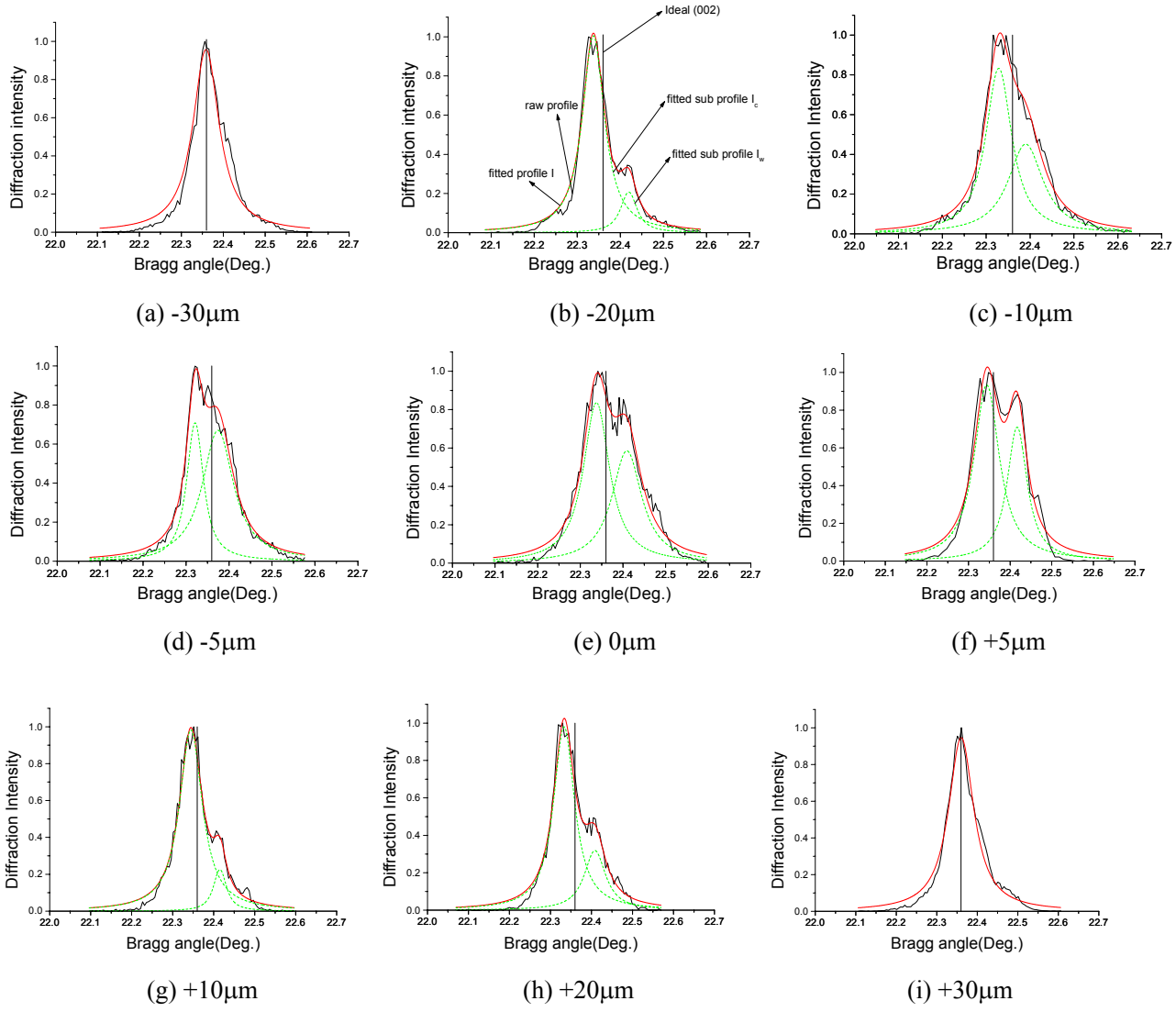

Figure 5. Spatial distribution of X-ray profile for (002) reflection of Al (001) sample Unsmoothed curve: raw profile, Smoothed curve: fitted profile, Dashed curves: two fitted sub profiles, Vertical line: ideal Bragg angle for Al (002) reflection (Diffraction intensity normalized).

If a piece of metal is deformed elastically such that the strain is uniform over a relatively large distance, the uniform macro-strain will cause a shift in the diffraction lines to new positions. If the metal is deformed plastically, such as in this case, the deformation creates adjacent regions of slight different orientations. The residual strain can vary from region to region to cause non-homogeneous strain state, which causes a broadening of the diffraction profile. In fact both kinds of strain are superposed in plastically deformed metals, and diffraction is both shifted and broadened [11]. It is the superposition that makes it difficult to evaluate the local strain and residual stress distribution.

However, on the basis of a composite model, local strain and residual stress can be evaluated for single crystal metal under plastic deformation as reported by Ungar [13] by recognizing that the crystal dislocations often arrange themselves in a cell structure. In the model, the deformed crystal is considered as a two-component system, where the local flow stress of the cell walls is considerably larger than the local flow stress of the cell interiors. Consequently, in the plastically deformed and unloaded crystals the cell walls parallel to the compressive axis are under a residual uniaxial compressive stress $\Delta\sigma_w$ <0 and the cell interior under a uniaxial tensile stress $\Delta\sigma_c$ >0. The asymmetrical Bragg reflections can be separated into the sum of two symmetrical peaks which correspond to "cell interiors" and "cell wall" as postulated by [13]. For brevity, the subscripts *w* and *c* will be used for walls and cell interiors. The integral intensities of the sub-profiles relative to the integral intensity of the measured profile are proportional to the volume fractions of the cell walls, f_w and cell interiors f_c=1-f_w, respectively. According to the model, stress equilibrium of the unloaded crystal requires:

$$f_w\Delta\sigma_w + (1-f_w)\Delta\sigma_c = 0 \tag{3}$$

The asymmetric line profiles *I* are assumed to be composed of two components I_w and I_c, where I_w is attributed to the cell-wall material (the integral intensity of which is proportional to f_w)and I_c to the cell-interior material(the integral intensity of I_c is proportional to $f_c = (1-f_w)$. The centers of both components are shifted in opposite directions in accordance with $\Delta\sigma_w$ <0 and $\Delta\sigma_c$ >0. These shifts can be expressed by the relative change of the mean lattice plane spacing $\Delta d/d$ as follows:

$$\left.\frac{\Delta d}{d}\right|_w = \frac{\Delta\sigma_w}{E} < 0\ ,\ \left.\frac{\Delta d}{d}\right|_c = \frac{\Delta\sigma_c}{E} > 0 \tag{4}$$

Where *E* is Young's modulus. We introduce a Cartesian coordinate system with the *z*-axis parallel to the stress axis and the *x*- and *y*-axes perpendicular to the two sets of walls that are parallel to the stress axis. Then, the measure of the residual stresses can be characterized by the absolute value of the difference

$$\sigma_{zz} = \left|\Delta\sigma_w - \Delta\sigma_c\right| \tag{5}$$

Their range of influence is of the order of the cell dimensions which is longer than the range of individual dislocations in a random distribution, e.g. in cell walls or in cell interiors. The lateral residual stress in the sample surface plane is

$$\sigma_{xx} = \sigma_{yy} = -\sigma_{zz}\cdot\nu \tag{6}$$

where *v* denotes Poisson's ratio.

6. X-RAY PROFILE ANALYSIS AND RESIDUAL STRESS EVALUATION

Consider the X-ray profile at 10μm left of the shocked line center as shown in details in Fig. 6. The raw profile represented by the unsmoothed curved is smoothed to obtain the fitted profile *I,* which is subsequently decomposed into two symmetric sub profiles I_c and I_w using Lorentzian peak function [14]. The centers of the decomposed sub-profiles are found to be shifted in opposite directions and the shifts can be related to the relative change of the mean lattice plane spacing $\Delta d/d$ of the corresponding lattice planes

$$\left.\frac{\Delta d}{d}\right|_{c\,(\text{or}\,w)} = -\cot\theta\ \Delta\theta_{c(\text{or}\,w)} \tag{7}$$

where $\Delta\theta_{c\,(\text{or}\,w)}$ is the angular shift of the sub-profiles I_c (or I_w) relative to the exact Bragg angle θ of the shock free regions. This equation is based on taking total differential of the Bragg law assuming perfect X-ray wavelength. For Al(002) reflection profile, the ideal Bragg angle corresponding to the shock free regions is θ=22.36°, the centers of gravity of the decomposed sub-profiles are θ_c=22.332°, and θ_w=22.384°, and therefore $\Delta\theta_c$=-0.028°, and $\Delta\theta_w$=0.024°. Consequently,

$$\left.\frac{\Delta d}{d}\right|_c = -\cot(22.36^\circ)(-0.028^\circ)(\pi/180) = 1.19\times10^{-3} \quad (8)$$

$$\left.\frac{\Delta d}{d}\right|_w = -\cot(22.36^\circ)(+0.024^\circ)(\pi/180) = -1.02\times10^{-3} \quad (9)$$

In the case of Al crystals, E=70 GPa and ν=0.33 and Eq. (4) gives

$$\Delta\sigma_c = E\cdot\left.\frac{\Delta d}{d}\right|_c = 83.3MPa \quad (10)$$

$$\Delta\sigma_w = E\cdot\left.\frac{\Delta d}{d}\right|_w = -72MPa \quad (11)$$

and Eq. (5) gives the axial residual stress $\sigma_{zz} = \left|\Delta\sigma_w - \Delta\sigma_c\right| = 155.3$ MPa and Eq. 6 gives the lateral residual stress within the sample surface plane

$$\sigma_{xx} = \sigma_{yy} = -\sigma_{zz}\cdot\nu = -51.2MPa \quad (12)$$

The volume fractions f_w and f_c of the walls and cell interiors can be obtained from the fractional integral intensities of the sub-profiles relative to the integral intensity of the total profile. Following the analysis method above for each measurement point (Fig. 5), the spatially resolved residual stress distribution is shown in Fig. 7. The simulation results from FEM as briefly explained in Section 3 are also superposed. First, the residual stresses are consistently compressive which is beneficial to fatigue life improvement [6]. The distributions show similar patterns and generally agree with each other. The lateral extent of the compressive residual stress is around ±30μm from the center of shocked line, while FEM results overestimate it. This is likely due to the pressure model used in the FEM which may have overestimated the lateral expansion effect of pressure loading on the sample surface [15].

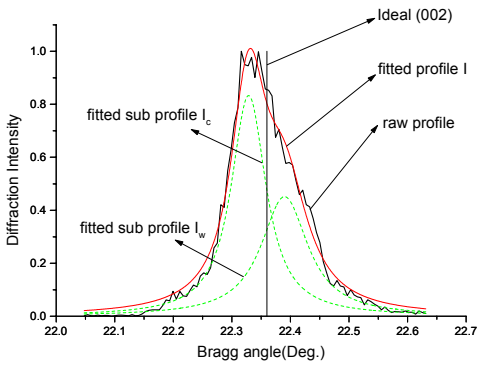

Figure 6. Detailed view of decomposition of asymmetric line profile

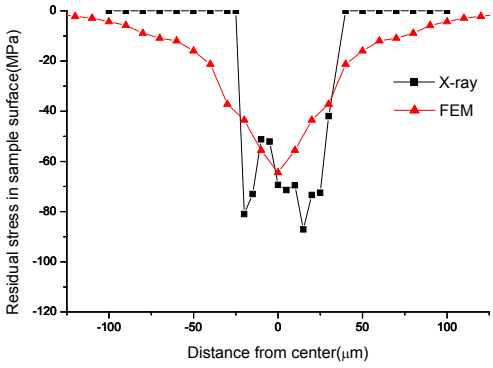

Figure 7. Distribution of residual stress on Al (001) sample surface

8. FURTHER UNDERSTANDING OF LSP INDUCED MICROSTRUCTURE CHANGE

The measurement is based on the postulation that LSP causes the formation of dislocation cell structure. From the recorded X-ray profile for the single crystal samples (Figs. 5), it strongly suggests the existence of dislocation cell structure. In fact, dislocation cell structures were observed via transmission electron microscopy (TEM) in laser shock penned metals [16]. This accompanies the generation and storage of a larger dislocation density during the shock process than for quasi-static processes.

Various models of dislocation patterning such as cell structure formation have been proposed that differ from the starting point, namely the driving force of this process. According to the thermodynamic approach, dislocation cells are considered as low energy structures [17]. This approach is, however, incorrect as energy minimization principles do not apply to dissipative processes far from equilibrium, such as dislocation glide during plastic deformation. In the synergetic theories developed by [18], the model considered the nonlinear dynamics of various dislocation densities, such as mobile, immobile and dipole dislocation configurations and focus on the evolution and dynamic stability of dipolar dislocation arrangements. An inherent weakness of this model relates to the neglect of long-range dislocation interactions.

In another model, it is assumed that the geometrically necessary effective stress fluctuations experienced by gliding dislocations cause appreciable fluctuations of the local strain rate. This enables the mobile dislocations to probe again and again new configurations. During this process, energetically favorable configurations possess a certain chance to become stabilized, whereas unfavorable arrangements are rapidly dissolved again. While cross slip supports this process by increasing the "selection pressure". That is, through increasing the range of possible slip planes, cross-slip increases the efficiency with which dislocations can move down energy gradients. From the stochastic dislocation dynamics model from [19], the critical condition for cell structure formation is:

$$\frac{<\tau^{\text{int}}>}{S} > (\frac{B_1}{B_2})^2 \frac{\rho}{\rho_m}\sigma_c^2(\phi) \tag{13}$$

where ρ_m and ρ_i are mobile and immobile dislocation densities, $\rho = \rho_m + \rho_i$ denotes the total dislocation density. τ^{int} is the long-range internal shear stress and the external resolved shear stress is τ^{ext}, the effective shear stress $\tau^{eff} = \tau^{ext} - \tau^{\text{int}}$ and it is the driving stress acting on a glide dislocation. The strain-rate sensitivity is defined as $S = \frac{\partial <\tau^{eff}>}{\partial \ln <\dot{\gamma}>}$, where $\dot{\gamma}$ is the local plastic shear strain rate. $\phi = \frac{<\tau^{eff}> + S}{\tau^{ext}}$ represents the additive noise in dislocation density change. The parameter B_1 describes the immobilization of dislocations (storages in the dislocation network), while B_2 accounts for the glide-induced dislocation annihilation. As annihilation is facilitated by cross slip, B_2 may increase with strain, while B_1 decreases, owing to an enhanced dynamic recovery by cross slip. Thus, the abundant cross slip is expected to lead a sharp decrease of B_1/B_2 so the cell formation condition is met. Also cross slip will increase the fraction of mobile dislocations so the dislocation cell formation is favored by easy cross slip.

8.1 PARTIAL DISLOCATION AND CROSS DISLOCATION IN FCC METALS

Consider a full slip vector in FCC metal, $(a/2)[\bar{1}01]$ shown in Fig. 8, the dissociation of a dislocation into two partials is favored on strain energy grounds because the total dislocation energy is reduced by the splitting. The vector components of two partial slips X and Y are $(a/6)[\bar{2}11]$ and $(a/6)[\bar{1}\,\bar{1}2]$, respectively. That is, the sum of dislocation energy (Gb^2) for the two partials is:

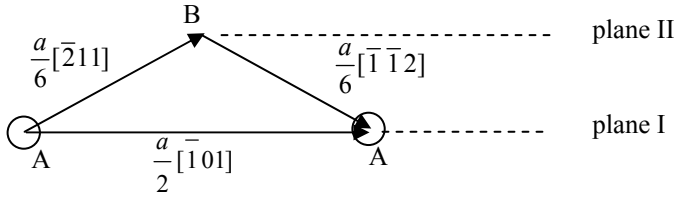

Figure 8. Partial dislocation in *FCC* metal

$$(Ga^2/36)(4+1+1) + (Ga^2/36)(1+1+4) = G\frac{a^2}{3} \tag{14}$$

while for the full dislocation, it is:

$$(Ga^2/4)(1+0+1) = G\frac{a^2}{2} \tag{15}$$

Thus, on strain energy considerations, the partial dislocation

$$\frac{a}{2}[\bar{1}01] = \frac{a}{6}[\bar{2}11] + \frac{a}{6}[\bar{1}\,\bar{1}2] \tag{16}$$

is expected.

For an edge dislocation, the Burgers vector is normal to the dislocation line and the two directions define the slip plane. However, for screw dislocation, the Burgers vector is parallel to the dislocation line, and thus, unlike for an edge dislocation, the Burgers vector and the screw dislocation line do not define a unique slip plane. The screw dislocation can be dissociated into cross-slips in different slip planes. In FCC metals, the $\{111\}$ family of planes contains common slip directions. For example the (111) and $(1\bar{1}1)$ planes have in common the direction $[\bar{1}01]$.

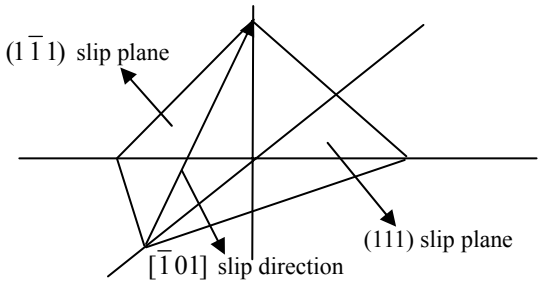

Figure 9.(b) Cross slip formation in *FCC* metal

Thus, if a screw dislocation traveling on a (111) plane in a FCC metal, and having a Burgers vector $(a/2)[\bar{1}01]$, encounters an obstacle on this plane, it can circumvent it by cross-slipping onto a $(1\bar{1}1)$ plane. Once the obstacle has been surmounted, the dislocation can then return, by an additional cross-slip process, to a (111) plane coplanar with the initial glide plane. Hence, a screw dislocation is able to overcome obstacles to slip by conservative motion involving cross-slip (Fig. 9). This is in contrast to the climb process required of edge dislocations for this purpose.

8.2 STACK FAULT ENERGY (SFE) IN FCC METAL AND ITS RELATION WITH PARTIAL SLIP AND CROSS SLIP

The most apparent feature controlling microstructures or microstructure development in FCC metals and alloys is the stacking-fault free energy. From Fig. 8, the atom A in slip plane I will move to a new position B through the two partial dislocations. This will result in atoms A in plane I temporarily occupying a B stacking sequence in the FCC lattice and the stacking fault occurs. Thus, if the SFE is high, partial dislocations will be difficult to occur. The SFE magnitude also controls the ease of cross-slip in FCC metals. As mentioned, cross-slip of screw dislocations can occur in FCC metals. However, as a result of a low SFE, a screw dislocation dissociates into partials and it contains edge components which can not cross-slip. Thus, FCC materials with low SFEs cross-slip with difficulty and vice versa.

From the analysis above, easy cross slip is an essential mechanism for dislocation cell formation. In high stacking-fault free energy materials, the stacking fault energy limits the partial dislocations and promotes cross slip of dislocations from one plane to another. So the high stacking-fault will favor the formation of dislocation cell structure. Typically, dislocation cell structures are formed in shock-loaded metals when the stacking-fault free energy is greater than about 60mJ/m^2 [16]. For stacking-fault free energy below about 40mJ/m^2, planar arrays of dislocations stacking faults, and other planar microstructures result. Al is the FCC metal with the highest stacking-fault free energy (168mJ/m2) and copper is 78mJ/m^2. As a result, the dislocation cell structure can be generated easier in material with higher stack fault energy.

9. CONCLUSIONS

Spatially resolved characterization of residual stress induced by micro scale laser shock peening was realized with X-ray micro-diffraction techniques for the first time. The asymmetric and broadened diffraction profiles registered at each location were analyzed by sub-profiling and explained in terms of the heterogeneous dislocation cell structure. For the first time, micron level spatial resolution (down to 5μm) of residual stress distribution in the surface of shock peened single crystal Al and Copper was achieved. The compressive residual stress is -80 to -100MPa within ±20μm from the shocked line center and it decreases very quickly to a few MPa beyond that range, which is indicative of the fact that the micro scale LSP has a very localized effect on material fatigue life enhancement. The results agree with FEM simulations. The asymmetric and double-peak profiles are strongly indicative of dislocation cell structure formation during LSP. Higher stack fault energy and easier cross slip favor the formation of cell structure. In general, it is shown that this technique is valuable in enabling spatially resolved residual stress quantification and in helping better understand microstructure change during the deformation process.

ACKNOWLEDGEMENT

This work is supported by the National Science Foundation under grant DMI-02-00334. Dr. Jean Jordan-Sweet and Dr. I. Cev Noyan in particular, of IBM Watson Research Center provided valuable guidance and permission to access X-ray microdiffraction apparatus at the National Synchrotron Light Source at Brookhaven National Laboratory.

REFERENCES

1. Clauer, A. H., and Holbrook, J. H., "Effects of Laser Induced Shock Waves on Metals," Shock Waves and High Strain Phenomena in Metals-Concepts and Applications, New York: Plenum, 1981: 675-702.
2. Zhang, W. and Yao, Y. L., "Improvement of Laser Induced Residual Stress Distributions via Shock Waves," *Proc. ICALEO'00, Laser Materials Processing*, Vol. 89: 2000; pp. E183-192.
3. Zhang, W. and Yao, Y. L., "Micro Scale Laser Shock Processing of Metallic Components," *ASME Journal of Manufacturing Science and Engineering*, Vol. 124, No. 2: 2000; pp. 369-378.
4. Noyan, I. C., Jordan-sweet J. L., Liniger, E. G., and Kaldor, S. K., "Characterization of Substrate / Thin-film Interfaces with X-ray Microdiffraction," *Applied Physics Letters*, Vol., 72(25): 1998; pp. 3338-3340.
5. Noyan, I. C., Wang, P. -C, Kaldor, S. K., and Jordan-sweet, J. L., "Deformation Field in Single-crystal

Semiconductor Substrates Caused by Metallization Features," *Applied Physics Letters*, Vol. 74(16): 1999; pp. 2352-2354.

6. Zhang, W. and Yao, Y. L., "Feasibility Study of Inducing Desirable Residual Stress Distribution in Laser Micromachining," *Transactions of the North American Manufacturing Research Institution of SME* (*NAMRC XXIX)* : 2001; pp. 413-420.
7. Wang, P. -C., Noyan, I. C., Kaldor, S. K., Jordan-sweet, J. L., Liniger, E. G., and Hu, C. -K., "Topographic Measurement of Electromigration-induced Stress Gradients in Aluminum Conductor Lines," *Applies Physic Letters*, Vol. 76(25): 2000; pp. 3726-3728.
8. Erko, A. I., Aristov, V. V., and Vidal, B., Diffraction X-ray Optics, Philadelphia: Institute of Physics Publishing Ltd, 1996: 2-15.
9. Cargill III, G. S., Hwang, K., Lam, J. W., Wang, P.-C., Linger, E., and Noyan, I. C., "Simulations and Experiments on Capillary Optics for X-ray Microbeams," *SPIE* Vol. 2516: 1995; pp. 120-134.
10. SPEC^{TM} X-ray Diffraction Software, Certified Scientific Software, Cambridge, MA.
11. Cullity, B. D., Elements of X-ray Diffraction, London: Addison-Wesley Publishing Company, Inc., Second edition, 1978: 268-270.
12. Noyan, I. C., Wang, P. -C, Kaldor, S. K., and Jordan-sweet, J. L., "Divergence Effects in Monochromatic X-ray Microdiffraction Using Tapered Capillary Optics," *Review of Scientific Instruments*, Vol. 71(5): 2000; pp. 1991-2000.
13. Ungar, T., *et al.*, "X-ray Line-Broadening Study of the Dislocation Cell Structure in Deformed [001]-Orientated Copper Single Crystals", *Acta ,etall*., Vol. 32, No. 3: 1984; pp. 332-342.
14. Noyan, I.C., and Cohen, J.B., Residual Stress-Measurement by Diffraction and Interpretation, New York: Springer-Verlag Inc., 1987:168-175.
15. Chen, H. Q., and Yao, Y. L., "Modeling Schemes, Transiency, and Strain Measurement for Microscale Laser Shock Processing", *ASME Journal of Manufacturing Processes*, submitted: 2003
16. Murr, L. E., "Microstructure-Mechanical Property Relations," Shock-wave and High-Strain-Rate Phenomena in Metals, New York: Plenum Press, Inc., 1981: 607-671.
17. Hansen, N., and Kuhlmann-Wilsdorf, D., "Proceedings of the International Conference on Low-Energy Dislocation Structures", *Materials Science and Engineering*, Vol. 81:1986; pp. 141-152.
18. Kratochvil, J., "Instability Origin of Dislocation Cell Misorientation", *Scripta Metallurgica et Materialia*, Vol. 24, No. 7: 1990; pp. 1225-1228.
19. Hahner, P, "A Theory of Dislocation Cell Formation Based on Stochastic Dislocation Dynamics", *Acta Mater.* , Vol. 44, No. 6: 1996; pp. 2345-2352.

Meet the authors:

Hongqiang Chen is a Ph.D candidate in the Department of Mechanical Engineering at Columbia University. He received a BS in 1997 and an MS in 2000 in Mechanical and Electrical Engineering from University of Science and Technology of China (USTC), P.R.China. His research interests are laser shock peening and laser micromachining. Y. Lawrence Yao is a Professor in the Department of Mechanical Engineering at Columbia University. He received his Ph.D. from the University of Wisconsin-Madison in 1988. He is interested in multidisciplinary research in manufacturing and design, nontraditional manufacturing processes and laser materials processing. He serves on the Board of Directors of LIA. Jeffrey W. Kysar is an Assistant professor in the Department of Mechanical Engineering at Columbia University. He received his Ph.D. from Harvard University in 1998 and his research interests are micromechanics of facture in ductile materials, and multi-scale experiments and modeling of fracture.